Graphene-supported small transition-metal clusters: A density functional theory investigation within van der Waals corrections

Celso R. C. Rêgo,[1,2] Polina Tereshchuk,[3] Luiz N. Oliveira,[1] and Juarez L. F. Da Silva[3,*]

[1]*São Carlos Institute of Physics, University of São Paulo, P.O. Box 369, 13560-970 São Carlos, SP, Brazil*

[2]*Amazonas State University, Avenida Djalma Batista 3578, Flores 69050-010, Manaus, AM, Brazil*

[3]*São Carlos Institute of Chemistry, University of São Paulo, P.O. Box 780, 13560-970 São Carlos, SP, Brazil*

(Received 3 April 2017; published 14 June 2017)

Transition-metal nanoparticles adsorbed on graphene are of great interest due to the unique catalytic and magnetic properties resulting from nanoparticles-graphene interactions. Comparison between the physical properties of such systems and those of the same nanoparticles in the gas phase is especially important. Here we report a systematic density functional investigation of the structural, energetic, and magnetic properties of small Ni_n, Pd_n, and Pt_n clusters, comprising from $n = 1$ to 6 atoms, in the gas phase and adsorbed on a graphene monolayer. Our results show that the Ni adatom binds to the graphene hollow site, with −1.47-meV adsorption energy, while Pd and Pt prefer the bridge sites, with −1.14- and −1.62-meV adsorption energies, respectively. This difference is determined by a competition between quantum and classical forces. Ni_2 and Pt_2 dimers bind perpendicularly on hollow and bridge sites, respectively, while Pd_2 lies parallel to the graphene sheet, with each adatom on a bridge site. For larger TM_n (TM = Ni, Pd, Pt; $n = 3$–6) clusters, either two or three atoms bind to bridge graphene sites. In almost all cases the adsorbed clusters retain their gas-phase structures. The exceptions are Ni_5 and Pt_4, which acquire more compact structures with effective coordination number 12 and 19% larger than in the gas phase, respectively. As the number of atoms grows, the cluster binds more weakly to the graphene, while its binding energy mounts up. Van der Waals corrections to the plain density functional theory (DFT) total energy raise the adsorption energy, but leave the cluster structure unchanged, in the gas phase or upon adsorption. Bader charge analysis shows that adsorption causes minor charge redistribution: the TM atoms bound to C atoms become positively charged, while the remaining metal atoms acquire negative charge. We have derived an approximate analytical expression for the local densities of states for the *d* orbitals of Ni, Pd, and Pt adatoms, on the basis of an extended Anderson-Newns model. Comparison with the DFT local densities of states for adsorption at hollow sites has identified interference among the wave functions responsible for the binding of distinct *d* levels to the C atoms. No such interference has become visible for adsorption at bridge sites.

DOI: 10.1103/PhysRevB.95.235422

I. INTRODUCTION

The number of unusual features in such physical properties as the transport coefficients and absorption spectrum of graphene [1,2] (Gr) makes this two-dimensional material unique among solids. The adsorption properties of the material being likewise extraordinary, transition-metal (TM) clusters on Gr support emerge as promising candidates for a wide range of applications, from catalysis to spintronics. For example, in many reactions the catalytic activity of TM atoms and nanoparticles adsorbed on Gr is much higher than that of standard catalysts, such as methanol oxidation [3], or hydrogenation of 1,3-butadiene [4]. Vacancies in Gr sheets supporting adsorbed TM clusters enhance their stability and chemical activity [5] and increase their hydrogen-storage capacity [6,7]. Yet another example is the large magnetic anisotropy of certain TM's, such as Co, adsorbed on Gr [8].

Various experimental approaches have recently yielded several stable TM adatoms, clusters, and nanoparticles on Gr sheets [3,9–11]. The resulting samples have been characterized via x-ray diffraction and spectroscopy, x-ray photoelectron spectroscopy, scanning tunneling microscopy (STM), and transmission electron microscopy [10,11]. For example, stable Ru and Rh nanoparticles on Gr in the 2- to 3-nm range resulted from decomposition of metal carbonyl precursors under rapid microwave irradiation of a Gr suspension in the ionic liquid 1-butyl-3-methylimidazolium tetrafluoroborate [9]. Another work described the formation of 5- to 40-atom Pt subnanoclusters on Gr nanosheets, which started with the ethanol reduction of H_2PtCl_6 and yielded compounds containing Pt^{II+} with particle sizes in the 2- to 7-nm range. Subsequent immersion in a H_2 atmosphere at 400°C generated Pt subnanoclusters [10]. In a morphological study of atomic Co and Fe adsorption on Gr, STM measurements showed that Co monomers adsorb on top [11]. Unfortunately, displacement of the adatom by the tip defeated the effort to determine the Fe adsorption site.

On the theoretical front, notwithstanding the number of reports, the influence of the Gr support on the properties of the TM clusters is poorly understood. Most density functional theory (DFT) investigations of Gr-supported TM clusters have been focused on the structure of TM-atom or small TM_n-cluster adsorption on Gr, with $n = 1$–4 or 5 atoms, and TM = Co [8,12], Au [13], Pt [14–16], Pd [17–19], Pt−Au alloys [20], and 3*d* TM atoms (TM = Fe, Co, Ni) [8,12,21,22]. The TM-adatom adsorption site on Gr has been found to depend strongly on the chemical specie. For example, 3*d* adatoms bind on the hollow sites [8,12,21], while Pd and Pt adatoms bind on the bridge sites [14,16–18]; Rudenko *et al.* [12] have identified two stable states of Co adatoms on Gr: the high-spin configuration ($3d^7\ 4s^2$, with $S = 3/2$), which is physisorbed,

*Corresponding author: juarez_dasilva@iqsc.usp.br

and the low-spin configuration ($3d^9$, with $S = 1/2$), associated with chemical bonding, i.e., strong orbital hybridization. For small clusters (e.g., Pt), the Pt−Pt binding has been found to be much stronger than the Pt−C binding, so that the cluster structure is preserved upon adsorption on Gr, while the magnetic moments, local spins, orbital moments, and magnetic-anisotropy energies of the adsorbed Pt clusters are much smaller than in the gas-phase clusters [14].

To our knowledge, the cluster-size dependence of structural and adsorption properties has never been systematically studied. In the case of Ni, for instance, only single-atom [21] and large-cluster ($n = 6$–9) [5] adsorptions have been considered. Moreover, different authors have reported contradictory findings on the cluster structure on the Gr sheet. For example, Ji *et al.* [20] and Cabria *et al.* [17] have found the Pd_2 dimer to bind by one atom, perpendicularly to the Gr sheet, while Thapa *et al.* [18] have shown that each Pd atom binds to a bridge site, so that the dimer axis is parallel to the sheet.

The findings by Błoński and Hafner [14] and Fampiou and Ramasubramaniam [16] on the Pt_2 and Pt_3 structures on Gr are similar, both describing an upright dimer and an upright triangle with one edge parallel to the sheet, respectively. By contrast, their reports on the structure of the Pt_4 cluster are distinct: a bent rhombus was found by Ref. [14] and a trigonal pyramid was found by Ref. [16]. Only the following larger-size clusters have been investigated: Pd−Au with $n = 7$ [23]; Co [24], Pt [25], Fe, Co, Ni [26], and MPd_{12} (M = Fe, Co, Ni, Cu, Zn, Pd) [27]; and Au_{49} [28].

These limitations, complexity, and controversies call for systematic study of TM_n clusters on the Gr sheet, to identify trends and classify the interactions between TM clusters and Gr. Here, we present a density functional investigation of the structural, adsorption, and magnetic properties of the TM_n (TM = Ni, Pd, Pt; $n = 1$–6) clusters on a Gr monolayer. To accurately describe the effect of van der Waals interactions on the geometry and electronic structure of the studied systems, we add van der Waals corrections to the ground-state energies. To probe the interactions we carry out Bader charge and density-of-states analyses. On the basis of the results, we propose a theoretical model that provides deeper understanding of the interaction between the TM and graphene atoms.

II. THEORETICAL APPROACH AND COMPUTATIONAL DETAILS

Our total-energy spin-polarized calculations were based on DFT [29,30] within the generalized-gradient approximation [31] (GGA) proposed by Perdew-Burke-Ernzerhof [32] (PBE) for the exchange-correlation (XC) functional. To compensate for the poor description of van der Waals (vdW) interactions by local [33,34] and semilocal XC functionals [35–39], we employed the a *posteriori* energy-dispersion correction $E_{\rm disp}$ proposed by Tkatchenko *et al.* (TS-SCS) [40], which takes into account the self-consistent screening (SCS) effects and acts in the whole system, e.g., Gr plus clusters. In the TS-SCS approach the electrostatic screening effect comes not only from local dipolar fluctuations as in the TS [41] scheme, but it is also due to the existence of a global interaction between local fluctuating dipoles with distant dipoles, which is computed self-consistently.

The total energy in the TS-SCS framework is the following equation, $E_{\rm tot} = E_{\rm tot}^{\rm DFT} + E_{\rm disp}$, where $E_{\rm tot}^{\rm DFT}$ is the plain DFT total energy, and $E_{\rm disp}$ is given by the following equation:

$$E_{\rm disp} = -\frac{1}{2}\sum_{A=1}^{N}\sum_{B=1}^{N}\sum_{L}{}' \frac{C_{6AB}}{r_{AB,L}^{6}} f_{\rm damp}(r_{AB,L}), \qquad (1)$$

where $r_{AB,L} = |r_A - r_B|$ is the atomic distance between the atoms A and B. The C_{6AB} parameters are the dispersion vdW coefficients for the atom pair AB. N denotes the numbers of atoms in the system, the index $L = (\ell_1,\ell_2,\ell_3)$, $r_{AB,L} = |r_A - (r_B + L)|$ counts the unit-cell translations, and the prime in the last summation means that for $L = 0$ A and B are not equal [41]. The damping function

$$f_{\rm damp}(r_{AB}) = (1 + \exp^{-d[r_{AB}/(sR_0)-1]})^{-1} \qquad (2)$$

is used to eliminate any divergency for very short distances r_{AB}, which must satisfy the following conditions $f_{\rm damp}(r_{AB} \to 0) = 0$ and $f_{\rm damp}(r_{AB} \to \infty) = 1$. Here, R_0 is the sum of the vdW radii of the two atomic species AB. The scaling factor s and the d parameter are dependent on the exchange-correlation functional only.

The dispersion coefficients and static polarizabilities are determined with reference to the atoms-in-molecules concept, i.e., from the corresponding quantities computed for free atoms and the proportionality between atomic volumes and polarizabilities. The atomic volumes are computed from Hirshfeld partitioning of the all-electron density [41,42]. The addition of electrodynamical response effects, such as the interaction of atomic electric dipole moments with the dynamic electric field due to the surrounding polarizable atoms, improves the accuracy of the vdW correction [37].

To solve the Kohn-Sham equations we applied the all-electron projected augmented wave (PAW) method [43,44], as implemented in the Vienna *ab initio* simulation package (VASP, version 5.3.3) [45,46], which employs plane waves to describe the Kohn-Sham orbitals under periodic boundary conditions. All total energies were computed with a 500-eV plane-wave cutoff, which is 17% higher than the largest recommended energy among the C (414eV), Ni (357eV), Pd (251eV), and Pt (249eV) PAW projectors. To improve the self-consistent electronic convergence, we employed a Gaussian smearing of 0.01eV. The Brillouin-zone integrations for the TM_n clusters in the gas phase used only the Γ point. For TM_n on Gr, using a (6×6) supercell, the integrations ran over a **k**-mesh of $3\times3\times1$.

To model the neutral TM_n (TM = Ni, Pd, Pt; $n = 1$–6) clusters in the gas phase, we employed a 16 Å cubic box. The resulting separation between clusters was at least 10Å, which ensured that the interaction between each cluster and its nearest image is negligible. To study the adsorption properties of the TM_n clusters on Gr, we employed the hexagonal (6×6) supercell with 72 C atoms depicted in Fig. 1. Consecutive Gr layers were separated by a 16 Å-wide vacuum region. For each unsupported and supported TM_n cluster, several atomic configurations were calculated to obtain a putative lowest-energy configuration. Molecular-dynamics simulations helped us identify the cation in the putative global minimum

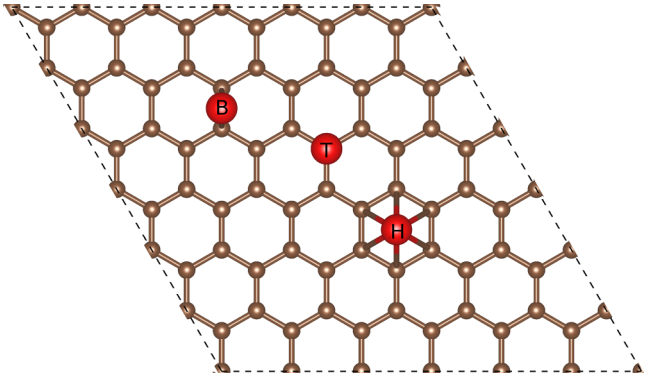

FIG. 1. Top view of the graphene (6×6) supercell, where the high-symmetry adsorption sites are indicated, namely, the one-fold top (T), two-fold bridge (B), and six-fold hollow (H) sites.

configurations (pGMC), an expedient that proved especially important for larger clusters. To determine all equilibrium PBE configurations we required the atomic force on every atom to be smaller than 0.025eVÅ, and the total energy to converge within of 1×10^{-6}eV. We reoptimized the lowest-energy configurations with the PBE+TS-SCS functional.

III. RESULTS AND DISCUSSION

A. Graphene and gas-phase clusters

1. Graphene

For the (6×6) Gr supercell, binding energies of −7.854, −7.857, and −7.858eV/atom resulted in $2 \times 2 \times 1$, $3 \times 3 \times 1$, and $6 \times 6 \times 1$ **k**-point meshes, respectively. We therefore selected the $3 \times 3 \times 1$ mesh, which provides the best compromise between accuracy and computational cost, for the subsequent calculations. The computed in-plane lattice parameter showed excellent agreement with experiment. We obtained $a_0 = 2.471$Å (PBE) for the graphene (1×1) lattice, only 0.37% larger than the experimental value (2.462Å) [47]. The strong localized covalent C-Csp^2 bond (5.23 eV/bond) makes the equilibrium distance insensitive to the vdW TS-SCS correction. Our result for a_0 is therefore consistent with the values in previous studies [37–39].

2. Gas-phase clusters

Figure 2 shows the pGMC's for Ni_n, Pd_n, and Pt_n clusters in the neutral state. The most important higher-energy isomers are described in Ref. [48]. Table I lists the binding energies per atom E_b, measured from the free-atom energies, the effective coordination numbers (ECN), relative to the number of nearest neighbors (NNN) [49,50], the average weighted bond lengths d_{av}, and the magnetic moments m_T.

For both Ni_n and Pd_n, compact structures, ranging from a perfect triangle for $n = 3$ (ECN = 2NNN) to a bipyramidal structure for $n = 6$ (ECN = 3.97NNN), proved to be most stable. By contrast, the studied Pt_n clusters showed strong preference for planar structures with smaller ECN's. The same behavior has been reported in small Au_n ($n < 14$) clusters. Given that relativistic effects tend to lower the energy of the 6*s* orbitals and raise that of the 5*d* electrons, and that the hybridization is stronger in the planar structures,

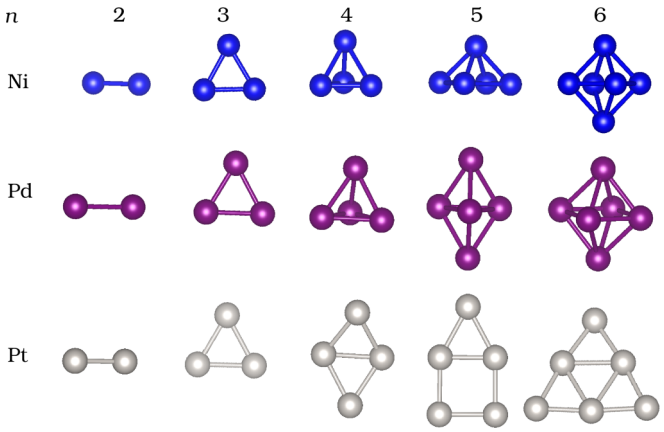

FIG. 2. Putative global minimum configurations for the neutral TM_n clusters (TM = Ni, Pd, and Pt; $n = 2$–6) in the gas phase obtained with the PBE functional.

it has been argued that such relativistic effects account for the planar structure of small Au and Pt clusters [51–55]. More recently, detailed analysis of the planar-to-globular transition in small gold clusters has convincingly questioned that argument [56]. The planar structures for Pt_n ($n = 4$–6) in Fig. 2, which resulted from nonrelativistic computations, support the conclusions in Ref. [56].

The average bond lengths and average effective coordination numbers grow with the cluster size n. Inspection of Table I reveals the following ordering of average bond lengths: $d_{av}^{Ni} < d_{av}^{Pt} < d_{av}^{Pd}$. To explain this sequence, we have to examine the two inequalities separately. To see that the first inequality mirrors the difference between the atomic radius of Ni and the radii of the other two atoms, we only have to recall that the lattice parameter in bulk Ni (3.52Å) is nearly 10% smaller than those in bulk Pd (3.89Å) or Pt (3.92Å) [57].

The same argument cannot explain the second inequality, however. The difference between the separations in bulk Pd and Pt is less than 1%. Moreover, the bulk data indicate that Pd is smaller than Pt, not larger. The inequality $d_{av}^{Pt} < d_{av}^{Pd}$ must therefore be due to a feature of the clusters not found in the bulk: the planarity of small Pt clusters. Had we considered clusters with larger sizes than the n in Table I, the Pt structure would have changed to globular, and the ordering in the bulk systems would have prevailed: $d^{Ni} < d^{Pd} < d^{Pt}$.

TABLE I. Gas-phase cluster properties. Binding energy per atom, $-E_b$; average effective coordination number, ECN, relative to the number of nearest neighbors; average bond length, d_{av}; and total magnetic moment, m_T, of the neutral Ni_n, Pd_n, and Pt_n clusters in the putative global-minimum configurations for gas-phase clusters.

	$-E_b$ (eV)			ECN (NNN)			d_{av} (Å)			m_T (μ_B)		
n	Ni	Pd	Pt	Ni	Pd	Pt	Ni	Pd	Pt	Ni	Pd	Pt
2	1.41	0.66	1.90	1.00	1.00	1.00	2.08	2.46	2.32	2.0	2.0	2.0
3	1.81	1.28	2.46	1.99	2.00	2.00	2.20	2.57	2.48	2.0	0.0	2.0
4	2.14	1.69	2.76	2.93	2.98	2.49	2.27	2.59	2.50	4.0	2.0	2.0
5	2.39	1.82	3.02	3.19	3.60	2.39	2.28	2.63	2.46	6.0	2.0	0.0
6	2.61	1.97	3.27	3.97	3.98	2.89	2.31	2.64	2.47	8.0	2.0	2.0

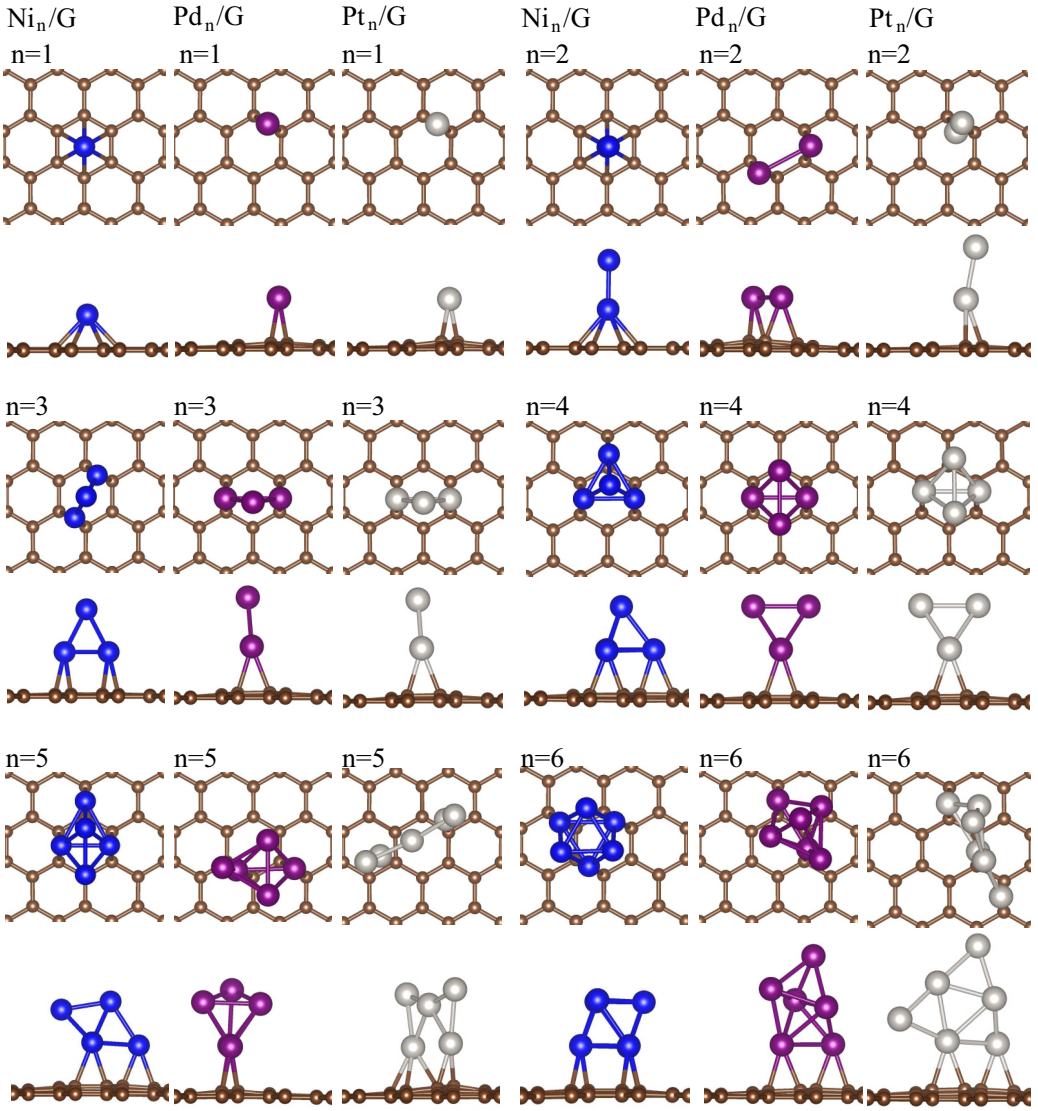

FIG. 3. Lowest-energy DFT-PBE configurations for neutral transition-metal clusters (TM$_n$; TM = Ni, Pd, and Pt; n = 1–6) on graphene, computed with a (6 × 6) supercell.

The results for d_{av} in Table I are in good agreement with previous results for Ni [58,59], Pd [60,61], and Pt [53,55] clusters, with the glaring exception of Ni_5 [62–64]. The computed magnetic moments for the Pd$_n$ and Pt$_n$ clusters are equal to $2\mu_B$, except that the moment vanishes for Pd_3 and Pt_5. The Ni$_n$ clusters possess larger magnetic moments, as expected, in the 2–8μ_B range. The magnetic moment is proportional to the number of unpaired d electrons and can be labeled by the multiplicity $2S + 1$ of the total spin S. Our calculations show that Ni$_n$ is in a triplet state for $n = 2$–3 and in quintet, septet, and nonet states for $n = 4,5$, and 6, respectively. Song *et al.* [58] report a heptet for $n = 6$, but otherwise our results agree well with their findings. In particular, the magnetic moments in our computations for $n = 3$ and 5 agree with theirs, rather than with the earlier computations in Ref. [65]. We identified singlet states for Pd $n = 2,3$ and triplets for $n = 4$–6, in disagreement with Ref. [66], which found triplets for $n = 2,5,6$, and quintuplets for $n = 3,4$. For Pt$_n$, we identified triplets for $n = 2,3,4,6$, and a singlet for $n = 5$, in disagreement with Kumar and Kawazoe [53], notwithstanding the agreement between the structures computed in Ref. [53] and here.

B. TM$_n$ clusters supported on graphene

The lowest-energy PBE and PBE+TS-SCS configurations for TM$_n$/Gr are nearly the same, i.e., only minor differences distinguish the computed structures; such behavior is expected, once the importance of SCS effects grows according to the cluster size [40]. We hence present only the PBE results in Fig. 3. The higher-energy structures and their total energies can be found in Ref. [48]. The most important structural parameters, adsorption energies, and magnetic properties for both the PBE and PBE+TS-SCS functionals are summarized in Table II and will be discussed in Sec. III B 1.

1. *Lowest-energy* TM$_n$Gr *configurations*

Our results show that Ni adatoms are most stable at the sixfold hollow sites. By comparison, binding to a single C atom at a top site raises the binding energy by 0.31eV. In contrast, Pd

TABLE II. Structural, energetic, and magnetic properties of transition-metal clusters (TM_n; TM = Ni, Pd, and Pt; n = 1–6) on graphene, calculated with the PBE and PBE+TS-SCS functionals. Listed are the most stable adsorption sites, the number N_b of TM atoms bound to the graphene sheet, the adsorption energy $-E_{ad}$ per TM atom, the binding energy $-E_b$, the minimum distance d_{min} between the TM_n cluster and the graphene sheet, the changes ΔECN in the average effective coordination number and in the average bond lengths Δd_{av} due to the adsorption on the graphene layer, and total magnetic moment.

TM	n	Site	N_b	$-E_{ad}$ (eV)	$-E_{ad}^{vdW}$ (eV)	$-E_b$ (eV)	$-E_b^{vdW}$ (eV)	d_{min} (Å)	d_{min}^{vdW} (Å)	ΔECN (%)	ΔECN^{vdW} (%)	Δd_{av} (%)	Δd_{av}^{vdW} (%)	m_T (μ_B)	m_T^{vdW} (μ_B)
Ni	1	Top		1.16	1.43	1.16	1.43	2.02	1.84	0.00		0.00		0.0	0.0
	1	Bridge		1.24	1.51	1.24	1.51	2.09	1.93	0.00		0.00		0.0	0.0
	1	Hollow		1.47	1.81	1.47	1.81	2.11	2.11	0.00	0.00	0.00	0.00	0.0	0.0
	2	Hollow	1	0.52	0.81	1.92	2.22	2.22	2.21	0.00	0.00	3.37	+2.94	2.0	2.0
	3	Bridge	2	0.55	0.83	2.37	2.64	2.05	2.04	+0.50	0.00	2.27	−2.07	2.0	1.9
	4	Bridge	3	0.48	0.73	2.62	2.87	2.03	2.02	+2.39	+1.59	2.20	+2.21	2.4	0.0
	5	Bridge	3	0.29	0.56	2.67	2.95	2.11	2.01	+11.91	−0.12	2.63	+1.52	4.0	4.0
	6	Bridge	3	0.16	0.41	2.77	3.05	2.03	2.02	+0.50	+0.33	1.30	+1.32	2.2	2.2
Pd	1	Hollow		0.92	1.14	0.92	1.14	2.39	2.43	0.00		0.00		0.0	
	1	Top		1.10	1.28	1.10	1.28	2.07	2.08	0.00		0.00		0.0	
	1	Bridge		1.14	1.34	1.14	1.34	2.09	2.17	0.00	0.00	0.00	0.00	0.0	0.0
						1.09[a,b]		2.22[a]							
						1.18[c]		2.18[c]							
	2	Bridge	2	0.73	0.92	1.39	1.59	2.13	2.14	0.00	0.00	3.47	+8.13	0.0	0.0
						1.28[a]		2.26[a]							
						1.10[c]		1.78[c]							
						1.29[d]	2.48[d]								
	3	Bridge	2	0.29	0.46	1.58	1.75	2.23	2.23	0.00	0.00	4.05	+3.54	1.6	1.6
						1.44[a]		2.29[a]							
	4	Bridge	2	0.23	0.40	1.93	2.09	2.28	2.27	−1.01	−0.97	0.39	+0.22	1.8	1.8
						1.84[a]		2.43[a]							
	5	Bridge	2	0.21	0.35	2.04	2.19	2.22	2.18	−1.67	−0.95	0.76	+1.02	1.6	1.6
						1.93[a]		2.43[a]							
	6	Bridge	2	0.14	0.27	2.12	2.25	2.19	2.19	−0.50	+0.74	0.76	+0.45	1.6	1.6
Pt	1	Hollow		0.88	1.19	0.88	1.19	2.40	2.39	0.00		0.00		0.0	
	1	Top		1.42	1.68	1.42	1.68	2.02	2.02	0.00		0.00		0.0	
	1	Bridge		1.62	1.88	1.62	1.88	2.09	2.09	0.00	0.00	0.00	0.00	0.0	0.0
						1.54[e]		1.54[e]		2.11[e]					
						1.57[f]				2.10[f]					
	2	Bridge	1	0.48	0.71	2.37	2.60	2.23	2.23	0.00	0.00	1.72	+1.31	1.8	1.8
				0.48[e]		2.38[e]									
				0.39[f]				2.38[f]							
	3	Bridge	2	0.48	0.73	2.94	3.17	2.23	2.23	−0.50	0.00	0.00	+1.09	0.0	0.0
				0.47[e]		2.95[e]									
				0.45[f]		2.49[f]									
	4	Bridge	2	0.38	0.60	3.12	3.35	2.22	2.21	+19.28	+16.23	3.20	+3.38	1.8	1.8
				0.31[e]		3.03[e]									
				0.28[f]				2.60[f]							
	5	Bridge-hollow	2	0.31	0.52	3.33	3.55	2.14	2.14	−0.42	−0.54	1.22	+1.23	2.0	2.0
				0.16[e]		3.20[e]									
	6	Bridge	2	0.11	0.30	3.38	3.59	2.15	2.15	−0.69	+0.74	1.61	+1.84	2.0	2.0

[a]GGA-PW91 [17].
[b]GGA-PW91 [19].
[c]GGA-PBE [18].
[d]GGA-PBE [20].
[e]GGA-PW91 [14].
[f]GGA-PBE [16].

and Pt adatoms bind to the graphene bridge sites, the binding to the top and hollow sites being less stable, higher in energy by 0.22 and 0.74eV, respectively. The energy differences favoring adsorption at the top site, relative to the hollow site, are −0.31, 0.18, and 0.54eV for Ni, Pd, and Pt, respectively. The larger the adatom radius, the more stable the top site. Our results are in good agreement with previous findings [14,16,18,21].

In the lowest-energy configurations of the TM_2 diatomic molecules, Ni_2 and Pt_2 bind perpendicularly to the graphene plane on the hollow and bridge sites, respectively. Only one of

the two TM atoms binds to the surface. By contrast, Pd_2 binds parallel to the graphene plane with each Pd atom on a bridge site. Our results for Pd_2 agree with the results by Ji *et al.* [20] and Cabria *et al.* [17], but disagree with another study [18], which concluded that the Pd_2 stands upright on the graphene sheet. Our results for Pt_2 agree well with those by Błoński and Hafner [14] and Fampiou and Ramasubramaniam [16].

For TM_3/Gr, the triangular clusters bind perpendicularly to the plane, at the bridge sites. More specifically, in the most stable configuration two of the three atoms bind to the plane. Configurations with the triangle flat on the Gr sheet have higher energy. For $n = 4$, the TM_n tetrahedrical clusters bind to the graphene with three, two, or two TM atoms for Ni_4, Pd_4, and Pt_4, respectively. We found the same numbers of bound atoms for Ni_n, Pd_n, and Pt_n with $n = 5$ and 6. The number of atoms that binds to the graphene sheet therefore remains fixed as the cluster size grows, an invariance that will be discussed below. For Pt_n ($n = 3$–6), our results are similar to those reported by Błoński and Hafner [14]. For Pd_n ($n = 3$–6), there is clear disagreement with the results by Cabria *et al.* [17].

For most clusters, the ECN and d_{av} are practically identical to those in the gas-phase clusters, the differences ranging from −1.67 to +2.39%. There are a few exceptions, however. For instance, upon adsorption the ECN's for Ni_5 and Pt_4 rise roughly 12 and 19%, i.e., from 3.19NNN and 2.49NNN to 3.57NNN and 2.97NNN, respectively. As these examples show, the cluster-graphene interaction tends to enhance the average coordination. Nonetheless, the bond lengths change by less than 0.1Å upon adsorption.

2. Adsorption and binding energies

To monitor the strength of the cluster-graphene interaction we calculated the adsorption energy per atom E_{ad} and the binding energy per atom E_b. Both E_{ad} and E_b are measured from the energies of the (infinitely separated) Gr sheet and gas-phase clusters:

$$E_{ad} = \frac{1}{n}\left(E_{tot}^{TM_n/Gr} - E_{tot}^{Gr} - E_{tot}^{TM_n}\right), \quad (3)$$

and

$$E_b = \frac{1}{n}\left(E_{tot}^{TM_n/Gr} - E_{tot}^{Gr} - nE_{tot}^{TM}\right), \quad (4)$$

where $E_{tot}^{TM_n/Gr}$, E_{tot}^{Gr}, $E_{tot}^{TM_n}$, and E_{tot}^{TM} are the total energies of the TM_n/Gr system, Gr plane, gas-phase TM_n cluster, and TM free atom, respectively, $E_{tot}^{TM_n/Gr}$ and E_{tot}^{Gr} being computed with the same unit cell. The results are listed in Table II.

With either the PBE or the PBE+vdW functionals, the magnitude $|E_{ad}|$ of the adsorption energy is reduced as the cluster size grows. The PBE computation of the adsorption energy for Ni_n, for instance, went down from 1.47eV/atom($n = 1$) to 0.16eV/atom($n = 6$). The reduction in the per-atom adsorption energy can be easily understood, since the number of TM atoms directly bound to the Gr sheet tends to saturate as n grows. However, the per-cluster adsorption energy nE_{ad}, a quantification of the cluster-graphene interaction, tends to decrease with n. This trend is due to the increased coordination of the TM atoms bound to the graphene.

In contrast with the adsorption energy, the binding energy per atom rises (in magnitude) with n. For Ni_n our PBE computation showed that, in analogy with the binding energies of the gas-phase clusters, $|E_b|$ grows with n, from 1.47eV/atom($n = 1$) to 2.77eV/atom($n = 6$). Relative to the binding energies in Table I, the binding energies of the supported clusters are slightly larger. For $n = 6$, for instance, the binding energy in Table I is 2.61eV/atom, while the corresponding energy in Table II is 2.77eV/atom($n = 6$). On intuitive grounds, in analogy with the reasoning that explains the binding energies of metallic systems, one would expect the binding energy to decrease upon adsorption, since the valence electrons of the n TM atoms are now shared among a larger number of bonds. The enhanced binding energies in Table II indicate that the adsorption also redistributes the valence electrons of the carbon bonds in the vicinity of the adsorption sites.

Comparison with the literature shows good agreement with the data for Pd_n/Gr and Pt_n/Gr. For example, our calculated E_b for Pd_n/Gr ($n = 1,2$) lie in the range of the published binding energies, which range from −1.09eV [17,19] to −1.18eV [18] for Pd_1/Gr, and from −1.10eV [18] to −1.29eV for Pd_2/Gr [17,20]. Our results slightly overestimate the energies obtained by Cabria *et al.* [17] with the GGA-PW91 functional, e.g., $|E_b| = 1.44$, 1.84, and 1.93eV for Pd_3/Gr, Pd_4/Gr, and Pd_5/Gr, respectively. Our findings for Pt_n/Gr ($n = 1$–6) agree very well with the data by Błoński and Hafner [14] ($|E_b| = 2.38$ to 3.20 eV and $|E_{ad}| = 1.54$ to 0.16 eV for Pt_n/Gr), while slightly overestimating the results of Fampiou and Ramasubramaniam [16].

3. Effect of van der Waals corrections

In most cases, the addition of vdW corrections to the total DFT energy has virtually no effect on the cluster structures in the gas phase, the average bond lengths and the ECN's changing by less than 0.01Å and 0.01NNN, respectively. There are two exceptions: Ni_5 becomes more compact, the ECN growing from 3.19 to 3.58NNN and the average bond length growing from 2.28 to 2.31Å, and Pd_2, the average ECN decaying from 2.59 to 2.47NNN. The TM_n clusters supported on graphene displayed a similar trend. The vdW corrections changed their ECNs and average bond lengths by less than 1%. The minimal distances d_{min} separating the clusters from the Gr sheet varied within the 0.00 to 0.50% range. Again, two exceptions were found: Ni_5 and Pd_5, for which d_{min} changed by 4.7 and 1.8%, respectively. As expected, the vdW correction enhances the adsorption energies. The enhancement grows with the cluster size, but it has weaker dependence on the TM element. $|E_{ad}|$, for example, is enhanced by a factor ranging from 1.23 to 2.56 for Ni_n as the size grows from $n = 1$ to 6. For Pd_n, the enhancement varies from 1.18 to 1.93 in the same range, and for Pt_n it varies from 1.16 to 2.37.

4. Bader charge

We relied on Bader charge analysis to determine the nature of the interaction between the TM_n clusters and graphene. To compute the Bader charge Q^{Bader} for every atom in each TM_n/Gr system we employed VASP high-density grids [67]. We calculated the average effective charge $\Delta Q^{TM\text{-}C} = Z_{val} - Q^{Bader}$, where Z_{val} and Q^{Bader} are the number of valence electrons and Bader charge on each atom, respectively. Table III presents the average effective charge on the TM atoms

TABLE III. Effective Bader charges in the TM_n/Gr systems, in units of the electronic charge e, calculated from $\Delta Q^{TM-C} = Z_{val} - Q^{Bader}$. Here ΔQ^{TM_b} and $\Delta Q^{TM_{unb}}$ are the effective charges on the TM atoms bound to and unbound from C atoms, respectively. ΔQ^{C_b} and $\Delta Q^{C_{unb}}$ are the total effective charges in C atoms bound to and unbound from TM atoms, respectively.

	ΔQ^{TM_b}			$\Delta Q^{TM_{unb}}$			ΔQ^{C_b}			$\Delta Q^{C_{unb}}$		
n	Ni	Pd	Pt	Ni	Pd	Pt	Ni	Pd	Pt	Ni	Pd	Pt
1	+0.525	+0.235	+0.056	0.000	0.000	0.000	−0.486	−0.149	−0.087	−0.039	−0.086	+0.032
2	+0.336	+0.359	+0.111	−0.133	0.000	−0.249	−0.479	−0.199	−0.126	+0.276	−0.159	+0.264
3	+0.564	+0.262	+0.355	−0.122	−0.141	−0.248	−0.382	−0.215	−0.224	−0.059	+0.094	+0.117
4	+0.865	+0.339	+0.352	−0.116	−0.119	−0.173	−0.578	−0.250	−0.258	−0.172	+0.030	+0.079
5	+0.802	+0.278	+0.331	−0.125	−0.058	−0.295	−0.573	−0.246	−0.259	−0.104	+0.025	+0.223
6	+0.762	+0.265	−0.105	−0.023	−0.025	+0.091	−0.597	−0.221	−0.228	−0.141	−0.018	+0.242

bound with C atoms, on the remaining TM atoms, and on the C atoms bound to TM atoms.

Our results show that the binding to the Gr sheet displaces a small electronic charge away from the TM atoms bound to the C atoms. The TM atoms therefore acquire positive charge, while negative charge is transferred to the C atoms directly bound to the cluster and to the other cluster atoms, the ones that are unbound from the C atoms. For example, in the Pt_n/Gr systems (n = 1–5) the charge on the TM atoms directly bound to C atoms lies in the $+0.06\,e$ to $+0.36\,e$ range. The charges of the C atoms bound to the TM atoms are in the $-0.09\,e$ to $-0.26\,e$ range.

The transfer is due to the unequal electronegativities [68] (1.91 for Ni, 2.28 for Pt, 2.20 for Pd, and 2.55 for C). The effective Bader charges ΔQ^{TM_b} and ΔQ^{C_b} in Table III correlate well with the electronegativity differences. The remaining charges, $\Delta Q^{TM_{unb}}$ and $\Delta Q^{C_{unb}}$, reflect redistributions imposed by two physical constraints: (i) overall, the TM_n/Gr system must have zero charge; and (ii) far from the adsorption site the electronic density must approach that of the Gr sheet.

5. *Density of states*

To describe the electronic properties of the studied systems we calculated the local densities of states (LDOS), such as s, p, and d states for all chemical species of the systems, i.e., C and TM atoms for pure Gr, gas-phase TM_n ($n = 2-6$) clusters, and TM_n/Gr (n = 1–6). Figure 4 displays the LDOS for TM_1/Gr. Results for TM_n/Gr (n = 2–6) can be found in the SI. The top panel of Fig. 4 displays the LDOS for a pure Gr sheet, showing C s states and C $p_x + p_y$ states lying deeply in the valence band, while the C p_z states, represented by the green line, are close the Fermi level, which controls the binding of the TM_n clusters. Upon adsorption of TM_n clusters, small peaks associated with C p_z states arise, while the overall C p_z peak amplitude decreases, as shown by the three lower panels, which display the LDOS for TM_1/Gr [TM = Ni (second panel), Pd (third panel), and Pt (bottom panel)]. These peaks are caused by the constructive and destructive interference between the d states of the impurity and C p_z orbital, and their magnitudes depend on the TM element. In the present paper, this effect is more prominent for the Ni interacting with Gr. The d-state LDOS in the three bottom panels display prominent peaks in the vicinity of the Fermi level and are similar to each other, even though the blue curve in the second panel is more tightly concentrated around the Fermi level than the purple and gray curves in the third and bottom panels, respectively.

IV. TM ADATOMS ON GRAPHENE

Our results for Ni_1/Gr show preference for the hollow site, followed by the bridge and top sites. The bridge site is the lowest-energy configuration for Pd_1/Gr and Pt_1/Gr, followed by the top and hollow sites. These results agree with previous findings [14,16,18,21]. In Table II for $n = 1$ the charge image effect is larger than the hybridization effect, which originates a chemical adsorption. However, for $n \geqslant 2$ the intracluster interactions decrease the charge transfer to Gr. Because of that, the hybridization effect become more important and their small adsorption energies are typical of physisorption. The covalent bonds between the p_z orbitals of carbon and the d_{z^2},

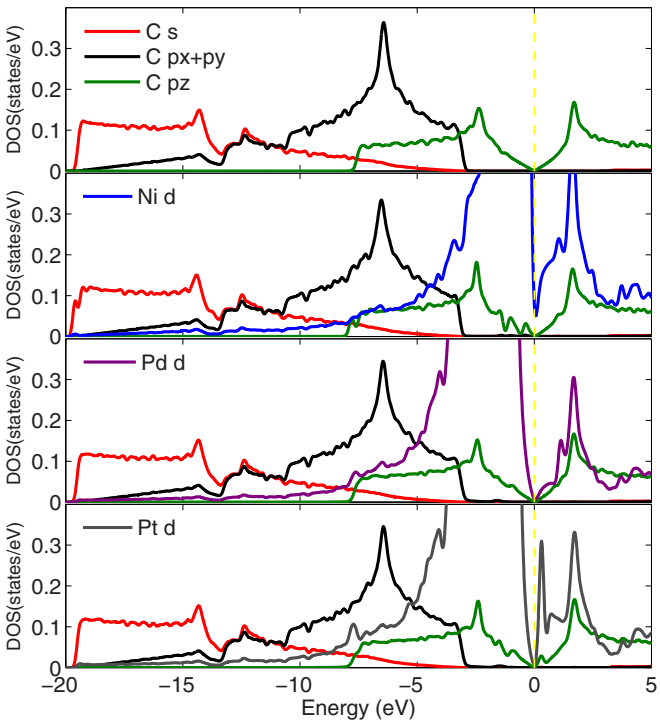

FIG. 4. Local densities of states (LDOS) for a single TM atom adsorbed on graphene. The top panel depicts Gr, while the second, third, and fourth panels refer to Ni_1/Gr, Pd_1/Gr, and Pt_1/Gr, respectively.

d_{xz}, and d_{yz} orbitals of the TM are weak. The tabulated energies show that $|E_{\rm ad}^{\rm Pt}| > |E_{\rm ad}^{\rm Ni}| > |E_{\rm ad}^{\rm Pd}|$.

The relatively small energy gained from adsorption at the bridge site in Pd_1/Gr is only 0.04eV higher than the energy from on-top adsorption. Given this small barrier separating two neighboring adsorption sites, we expect Pt to be mobile on Gr. The barriers between the hollow and bridge sites in Ni_1/Gr and between the bridge and top sites in Pt_1/Gr, approximately 0.2eV each, are sufficiently high to pin the adsorbates to the most stable sites. The binding to the hollow site distinguishes Ni/Gr from the other two systems. The preference of the hollow or the bridge site is determined by the competition between quantum and classical forces: the tendency to form chemical bonds and the image-charge attraction from the Gr layer. The latter pulls the adsorbed atom towards the plane through the Gr lattice sites and hence tends to bring small atoms to the open space surrounded by six C atoms.

Two factors therefore combine to favor Ni adsorption at the hollow size. The charge $0.525\,e$ on the Ni atom enhances the image-charge potential, and the small radius of the transition metal allows accommodation close to the lattice plane, which further strengthens the electrostatic attraction. From the data in Table II and the C atomic radius, simple geometry yields a distance $d = 2.0$Å between the Ni atom and the plane, which corresponds to an 0.94 eV image-charge energy, a large fraction of the Ni_1 adsorption energy. As the cluster size n grows the charge transferred to the bonded Ni atoms decreases. For $n > 2$ it becomes preferable to bind two or three atoms at bridge sites instead of having a single atom at a hollow site. By contrast with Ni, neither the transferred charges nor the atomic radii favor adsorption of Pd or Pt at hollow sites. The two atoms are bigger and the transferred charges, listed in Table III, are $0.235\,e$ (Pd) and $0.056\,e$ (Pt). Even for $n = 1$, therefore, Pd_n/Gr and Pt_n/Gr are more stable at bridge sites.

In an effort to describe the TM d-orbital LDOS's in Fig. 4 in more detail, we now compare the numerical results with the predictions of a simple theoretical model. Traditionally, the adsorption of atoms on metallic surfaces has been described by the Anderson-Newns model [69,70], in which the metal is represented by a noninteracting, structureless, half-filled band, and the adatom is represented by a single level coupled to the conduction band. Prior to discussing generalizations of the model to describe adsorption on Gr, brief recapitulation of its characteristics seems warranted.

Mathematically, the Anderson-Newns model is expressed by the Hamiltonian

$$H = E_{\mathbf{d}} d^\dagger d + \sum_{\mathbf{k}} \epsilon_{\mathbf{k}} c_{\mathbf{k}}^\dagger c_{\mathbf{k}} + \sum_{\mathbf{k}} (V_{\mathbf{k}} d^\dagger c_{\mathbf{k}} + \text{H.c.}). \quad (5)$$

The adatom energy $E_{\mathbf{d}}$ is shifted, relative to the atomic level, by the image potential induced on the metal by the ionized particle. In Eq. (5), the Fermi operator c_d ($c_{\mathbf{k}}$) annihilates an electron at the adatom level (at a conduction level with momentum k). The first and second terms on the right-hand side represent the adatom and the metal, respectively, and the last term is the momentum-dependent coupling between the two subsystems. The energies $\epsilon_{\mathbf{k}}$ define the dispersion relation for the metal.

The single-particle Hamiltonian in Eq. (5) is easily diagonalized. The LDOS ρ_{dd} for the c_d level can be obtained from the expression

$$\rho_{dd}(\omega) = -\frac{1}{\pi} \text{Im}[G^R(\omega)], \quad (6)$$

where $G^R(\omega)$ is the retarded Green's function:

$$G^R(\omega) = \frac{1}{\omega - E_d - \Sigma_d(\omega)}. \quad (7)$$

Here $\Sigma_d(\omega)$ is the c_d-level self-energy, due to the hybridization between the adatom and conduction levels.

The self-energy is given by the expression

$$\Sigma_d(\omega) = \sum_{\mathbf{k}} \frac{|V_{\mathbf{k}}|^2}{\omega - \epsilon_{\mathbf{k}} + i\eta}, \quad (8)$$

where η is a positive infinitesimal. The real part $\Sigma_R(\omega)$ of the self-energy shifts the adatom energy $E_{\mathbf{d}}$, while its imaginary part $\Delta_{\mathbf{d}}(\omega)$ broadens $E_{\mathbf{d}}$. Substitution of Eq. (7) on the right-hand side of Eq. (7) yields the following expression for the c_d-level LDOS:

$$\rho_{dd}(\omega) = \frac{1}{\pi} \frac{\Delta_{\mathbf{d}}(\omega)}{\left[\omega - E_d - \Sigma_R(\omega)\right]^2 + \Delta_{\mathbf{d}}^2(\omega)}. \quad (9)$$

Margulis and Muryumin [71] have extended the Anderson-Newns model to discuss hydrogen adsorption on Gr. In essence, the extension amounts to (i) substituting two bands with the Gr dispersion relation for the second term on the right-hand side of Eq. (5) and (ii) defining the momentum-dependent couplings V_k to describe binding to a bridge (B), hollow (H), or top (T) site. For each site, the self-energy can then be computed from Eq. (8), with the following results:

$$\Delta_{\mathbf{d}}^B(\omega) = \alpha_1 2|\omega|[1 - 0.5 J_0(\omega)], \quad (10a)$$

$$\Delta_{\mathbf{d}}^H(\omega) = \alpha_1 6|\omega|[1 - J_0(\omega)], \quad (10b)$$

$$\Delta_{\mathbf{d}}^T(\omega) = \alpha_1 |\omega|, \quad (10c)$$

$$\Sigma_R^B(\omega) = \alpha_2 \omega \left[2 g_c \ln \left| \frac{\omega}{\omega_c} \right| - (\pi/2) N_0(|\omega|) \right], \quad (11a)$$

$$\Sigma_R^H(\omega) = \alpha_2 \omega \left[6 g_c \ln \left| \frac{\omega}{\omega_c} \right| - 3 N_0(\sqrt{3}|\omega|) \right], \quad (11b)$$

$$\Sigma_R^T(\omega) = \alpha_2 g_c \omega \ln \left| \frac{\omega}{\omega_c} \right|. \quad (11c)$$

Here $\alpha_1 = \sqrt{3}|V_0|^2/|V_{pp\pi}|$, and $\alpha_2 = 2\alpha_1/\pi$, where $V_{pp\pi} = -3.03$eV is the π-electron transfer integral for clean graphene. J_0 and N_0 are the zeroth-order Bessel and Neumann functions, respectively. V_0 is an adjustable parameter defining the strength of the hybridization [69,70]. The cutoff energy ω_c is equal to $0.30\pi/\sqrt{3}$, and the cutoff function $g_c(\omega)$ is the Lorentzian:

$$g_c(\omega) = \frac{\omega_c^2}{\omega^2 + \omega_c^2}. \quad (12)$$

Description of TM adsorption on Gr calls for additional modification. The electronic configurations of the metals

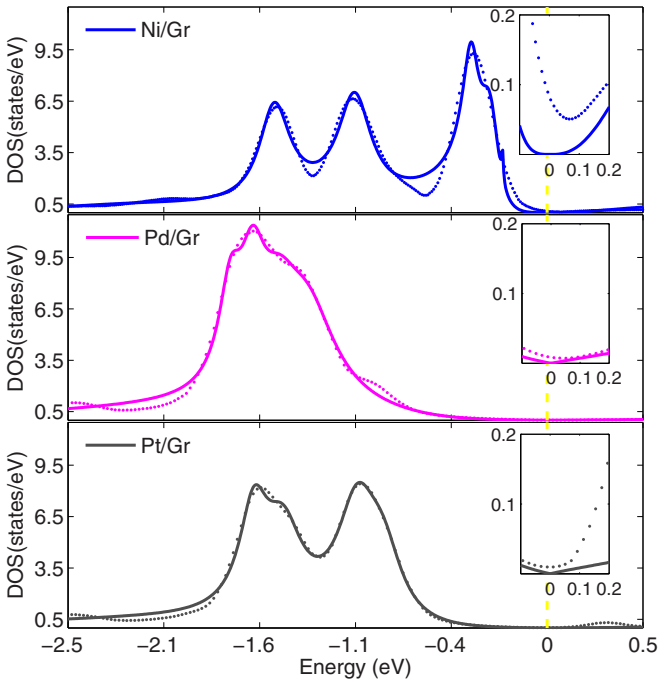

FIG. 5. Fits of the LDOS in Fig. 4 with the spectral density for the Anderson-Newns model described in the text. The open circles describe the adatom LDOS for the indicated systems, and the solid lines represent Eq. (13) with the parameters in Table IV. The insets show that, in contrast with numerical data, the right-hand side of Eq. (13) vanishes at zero energy. The vertical dashed line marks the Fermi level, from which energies are measured.

in our computation, Ni = [Ar]$3d^8 4s^2$, Pd = [Kr]$4d^{10}$, and Pt = [Xe]$4f^{14}5d^9 6s^1$, all with ten electrons in the valence band, are poorly described by the LDOS in Eq. (6), which covers a unit area. We have therefore fitted our numerical results with a combination of LDOS's analogous to Eq. (6), i.e., with the generalized form

$$\rho_{dd}(\omega) = \sum_{j=1}^{N} \frac{\beta_j \Delta_{\mathbf{d}}^j(\omega)/\pi}{\left[\omega - E_d^j - \Sigma_R^j(\omega)\right]^2 + \left[\Delta_{\mathbf{d}}^j(\omega)\right]^2}, \qquad (13)$$

where $N = 5$, the β_j and E_d^j are adjustable parameters, and the $\Sigma_R^j(\omega)$ [$\Delta_{\mathbf{d}}^j(\omega)$] are given by one of Eqs. (10) [Eqs. (11)], according to the adsorption site, with adjustable coefficients α_1^j substituted for the α_1 on the right-hand sides.

Figure 5 shows the resulting fits. The fitting parameters are listed in Table IV. As the main plots show, the model LDOS's reproduce the peak positions and widths, but miss the marked dips around $\epsilon = -0.6$eV and -1.2eV in the Ni/Gr dotted curves in the first panel of Fig. 5. The peaks represent the resonances resulting from the coupling between each adatom level and the Gr states. The discrepancies in the top panel indicate that the two dips are due to destructive interference between the resonances associated with the coupling of the Ni adatom and the C adatom around the hollow site, a partial cancellation that the superposition of spectral densities on the right-hand side of Eq. (13) cannot reproduce. No comparable interference is observed at the bridge sites, as indicated by the better agreement, in the same energy range, between the numerical and the analytical Pd/Gr and Pt/Gr curves in the second and third panels, respectively.

TABLE IV. Adjustable parameters on the right-hand side of Eq. (13). E_d^j and α_1 define the frequency and width of each resonance, while β_j defines the strength of the resonance.

TM	Adsorption site	j	β_j	E_d^j	$\lvert V_0^j \rvert$
Ni	Hollow	1	0.77	−4.59	0.15
		2	0.79	−1.62	0.45
		3	0.01	−1.06	0.28
		4	0.43	−1.87	0.24
		5	0.65	−6.41	0.16
Pd	Bridge	1	0.91	−6.27	0.32
		2	1.00	−5.48	0.35
		3	0.69	−6.98	0.25
		4	0.23	−14.69	0.37
		5	0.49	−7.55	0.22
Pt	Bridge	1	0.78	−6.17	0.31
		2	0.78	−4.48	0.29
		3	0.30	−15.00	0.43
		4	0.50	−3.94	0.31
		5	0.71	−6.95	0.26

The insets in Fig. 5 are magnifications of the regions around the Fermi level. While the analytical LDOS's vanish at $\epsilon = 0$, the dotted lines representing the numerical data have positive minima at positive energies. For the Anderson-Newns model, which represents a single adatom adsorbed on an infinite Gr monolayer, $\rho_{dd}(\epsilon = 0)$ must be zero, because the Gr density of states vanishes at the tip of the Dirac cones. In the DFT computation, by contrast, the charge transferred from the periodic array of TM adatoms to the C atoms raises the Fermi level to an energy above the Dirac singularity. The minimum LDOS in each panel is therefore controlled by the charge transferred between the adsorbed atom and the C atoms. The progressively smaller inset minima agree well with transferred charges in Table III, which shrink from 0.53 e (Ni/Gr) to 0.24 e (Pd/Gr) and 0.06 e (Pt/Gr) as one moves down from the top to the bottom panels in Fig. 5.

V. CONCLUSION

We have carried out an *ab initio* density functional investigation of the structural, energetic, and magnetic properties of one- to six-atom Ni, Pd, and Pt clusters on graphene. With a few exceptions, adsorption preserves the structure of the gas-phase clusters. As n grows, the interaction between the TM_n clusters and Gr weakens. The interaction is strongest for Ni and weakest for Pd and hence weakens as the d-orbital occupation grows. The vdW correction in our paper had little effect upon the TM_n cluster structures, either in the gas phase or adsorbed on Gr. Nonetheless, as expected, the corrections raise the adsorption energy. Our results show that, like the adsorption energy itself, the vdW contribution to the adsorption energy grows with cluster size and decreases with the number of d electrons.

Adsorption results in charge transfer between the TM_n clusters and Gr. The charge transfer from the TM atoms directly coupled to C atoms is controlled by the electronegativity

difference. Typically, the charge transfer between Ni and C is twice (three times) as large as the transfer between Pd (Pt) and C. In almost all studied systems, negative charge is transferred from the bound TM atoms to the C atoms. The exception is Pt_6, in which Pt acquires a small negative charge. In all cases, the charge on the remaining cluster atoms partially compensates for the charge lost by the bound TM atoms.

In order to find a different way to explore the physics involved in adsorption of the TM_n on Gr, we have used a modified Anderson-Newns model to describe the coupling between the two. Analysis of the agreement between the c_d-level LDOS resulting from the model and the DFT computations identified destructive interference between the resonances resulting from (Ni) adsorption on hollow sites, but no interference when the TM atom is adsorbed on bridge sites (Pd_1/Gr or Pt_1/Gr).

ACKNOWLEDGMENTS

This paper received financial support from the FAPESP, CNPq (Grant No. 312658/2013-3), and Brazilian National Program for Post-Doctoral Researchers (PNPD/CAPES). Infrastructural support from the Centro de Informática de São Carlos of the University of São Paulo is gratefully acknowledged.

[1] J. Baringhaus, M. Ruan, F. Edler, A. Tejeda, M. Sicot, A. Taleb-Ibrahimi, A.-P. Li, Z. Jiang, E. H. Conrad, C. Berger, C. Tegenkamp, and W. A. de Heer, Nature (London) **506**, 349 (2014).
[2] J. Jobst, D. Waldmann, F. Speck, R. Hirner, D. K. Maude, T. Seyller, and H. B. Weber, Phys. Rev. B **81**, 195434 (2010).
[3] E. Yoo, T. Okata, T. Akita, M. Kohyama, J. Nakamura, and I. Honma, Nano Lett. **9**, 2255 (2009).
[4] H. Yan, H. Cheng, H. Yi, Y. Lin, T. Yao, C. Wang, J. Li, S. Wei, and J. Lu, J. Am. Chem. Soc. **137**, 10484 (2015).
[5] W. Gao, J. E. Mueller, J. Anton, Q. Jiang, and T. Jacob, Angew. Chem. Int. Ed. **52**, 14237 (2013).
[6] A. Granja, J. A. Alonso, I. Cabria, and M. J. López, RSC Adv. **5**, 47945 (2015).
[7] C. M. Ramos-Castillo, J. U. Reveles, R. R. Zope, and R. de Coss, J. Phys. Chem. C **119**, 8402 (2015).
[8] F. Donati, Q. Dubout, G. Autès, F. Patthey, F. Calleja, P. Gambardella, O. V. Yazyev, and H. Brune, Phys. Rev. Lett. **111**, 236801 (2013).
[9] D. Marquardt, C. Vollmer, R. Thomann, P. Steurer, R. Mülhaupt, E. Redel, and C. Janiak, Carbon **49**, 1326 (2011).
[10] R. Siburian and J. Nakamura, J. Phys. Chem. C **116**, 22947 (2012).
[11] T. Eelbo, M. Waśniowska, P. Thakur, M. Gyamfi, B. Sachs, T. O. Wehling, S. Forti, U. Starke, C. Tieg, A. I. Lichtenstein, and R. Wiesendanger, Phys. Rev. Lett. **110**, 136804 (2013).
[12] A. N. Rudenko, F. J. Keil, M. I. Katsnelson, and A. I. Lichtenstein, Phys. Rev. B **86**, 075422 (2012).
[13] M. Amft, B. Sanyal, O. Eriksson, and N. V. Skorodumova, J. Phys.: Condens. Matter **23**, 205301 (2011).
[14] P. Błoński and J. Hafner, J. Chem. Phys. **134**, 154705 (2011).
[15] P. Błoński and J. Hafner, J. Chem. Phys. **137**, 044710 (2012).
[16] I. Fampiou and A. Ramasubramaniam, J. Phys. Chem. C **116**, 6543 (2012).
[17] I. Cabria, M. J. López, and J. A. Alonso, Phys. Rev. B **81**, 035403 (2010).
[18] R. Thapa, D. Sen, M. K. Mitra, and K. K. Chattopadhyay, Physica B **406**, 368 (2011).
[19] M. J. López, I. Cabria, and J. A. Alonso, J. Phys. Chem. C **118**, 5081 (2014).
[20] W.-X. Ji, C.-W. Zhang, F. Li, P. Li, P.-J. Wang, M.-J. Ren, and M. Yuan, RSC Adv. **4**, 55781 (2014).
[21] M. Sargolzaei and F. Gudarzi, J. Appl. Phys. **110**, 064303 (2011).
[22] C. D. Porter and D. Stroud, Phys. Rev. B **85**, 235452 (2012).
[23] D. W. Yuan, C. Liu, and Z. R. Liu, Phys. Lett. A **378**, 408 (2014).
[24] L. Liu, Y. Su, J. Gao, and J. Zhao, Physica E **46**, 6 (2012).
[25] D.-H. Lim and J. Wilcox, J. Phys. Chem. C **115**, 22742 (2011).
[26] S. Sahoo, M. E. Gruner, S. N. Khanna, and P. Entel, J. Chem. Phys. **141**, 074707 (2014).
[27] X. Liu, C. Meng, and Y. Han, J. Phys. Chem. C **117**, 1350 (2013).
[28] P. V. C. Medeiros, G. K. Gueorguiev, and S. Stafström, Phys. Rev. B **85**, 205423 (2012).
[29] P. Hohenberg and W. Kohn, Phys. Rev. **136**, B864 (1964).
[30] W. Kohn and L. J. Sham, Phys. Rev. **140**, A1133 (1965).
[31] J. P. Perdew, J. A. Chevary, S. H. Vosko, K. A. Jackson, M. R. Pederson, D. J. Singh, and C. Fiolhais, Phys. Rev. B **46**, 6671 (1992).
[32] J. P. Perdew, K. Burke, and M. Ernzerhof, Phys. Rev. Lett. **77**, 3865 (1996).
[33] J. L. F. Da Silva, C. Stampfl, and M. Scheffler, Phys. Rev. B **72**, 075424 (2005).
[34] J. L. F. Da Silva and C. Stampfl, Phys. Rev. B **76**, 085301 (2007).
[35] S. Kristyán and P. Pulay, Chem. Phys. Lett. **229**, 175 (1994).
[36] S. Grimme, J. Comput. Chem. **27**, 1787 (2006).
[37] T. Bučko, S. Lèbegue, J. Hafner, and J. G. Ángyán, Phys. Rev. B **87**, 064110 (2013).
[38] C. R. C. Rêgo, L. N. Oliveira, P. Tereshchuk, and J. L. F. Da Silva, J. Phys.: Condens. Matter **27**, 415502 (2015).
[39] C. R. C. Rêgo, L. N. Oliveira, P. Tereshchuk, and J. L. F. Da Silva, J. Phys.: Condens. Matter **28**, 129501 (2016).
[40] A. Tkatchenko, R. A. DiStasio, R. Car, and M. Scheffler, Phys. Rev. Lett. **108**, 236402 (2012).
[41] A. Tkatchenko and M. Scheffler, Phys. Rev. Lett. **102**, 073005 (2009).
[42] F. De Proft, R. Vivas-Reyes, A. Peeters, C. V. Alsenoy, and P. Geerlings, J. Comput. Chem. **24**, 463 (2003).
[43] P. E. Blöchl, Phys. Rev. B **50**, 17953 (1994).
[44] G. Kresse and D. Joubert, Phys. Rev. B **59**, 1758 (1999).
[45] G. Kresse and J. Furthmüller, Phys. Rev. B **54**, 11169 (1996).
[46] J. Hafner, J. Comput. Chem. **29**, 2044 (2008).
[47] Y. X. Zhao and I. L. Spain, Phys. Rev. B **40**, 993 (1989).
[48] See Supplemental Material at http://link.aps.org/supplemental/10.1103/PhysRevB.95.235422 for additional data, density of states, and all calculated atomic structure configurations. .

[49] R. Hoppe, Z. Kristallogr. **150**, 23 (1979).
[50] J. L. F. Da Silva, J. Appl. Phys. **109**, 023502 (2011).
[51] H. Häkkinen, M. Moseler, and U. Landman, Phys. Rev. Lett. **89**, 033401 (2002).
[52] L. Xiao and L. Wang, Chem. Phys. Lett. **392**, 452 (2004).
[53] V. Kumar and Y. Kawazoe, Phys. Rev. B **77**, 205418 (2008).
[54] P. Błoński, S. Dennler, and J. Hafner, J. Chem. Phys. **134**, 034107 (2011).
[55] A. S. Chaves, G. G. Rondina, M. J. Piotrowski, P. Tereshchuk, and J. L. F. Da Silva, J. Phys. Chem. A **118**, 10813 (2014).
[56] A. Kinaci, B. Narayanan, F. G. Sen, M. J. Davis, S. K. Gray, S. K. R. S. Sankaranarayanan, and M. K. Y. Chan, Sci. Rep. **6**, 34974 (2016).
[57] C. Kittel, *Introduction to Solid State Physics*, 8th ed. (Wiley, New York, 2004).
[58] W. Song, W.-C. Lu, C. Z. Wang, and K. M. Ho, Comput. Theor. Chem. **978**, 41 (2011).
[59] P. Calaminici, J. Chem. Phys. **128**, 164317 (2008).
[60] J. Rogan, G. García, J. A. Valdivia, W. Orellana, A. H. Romero, R. Ramírez, and M. Kiwi, Phys. Rev. B **72**, 115421 (2005).
[61] C. Luo, C. Zhou, J. Wu, T. J. D. Kumar, N. Balakrishnan, R. C. Forrey, and H. Cheng, Int. J. Quantum Chem. **107**, 1632 (2007).
[62] F. A. Reuse and S. N. Khanna, Chem. Phys. Lett. **234**, 77 (1995).
[63] M. Castro, C. Jamorski, and D. R. Salahub, Chem. Phys. Lett. **271**, 133 (1997).
[64] P. Błoński and J. Hafner, J. Phys.: Condens. Matter **23**, 136001 (2011).
[65] N. S. Venkataramanan, R. Sahara, H. Mizuseki, and Y. Kawazoe, J. Phys. Chem. A **114**, 5049 (2010).
[66] J.-Q. Wen, T. Xia, H. Zhou, and J.-F. Wang, J. Phys. Chem. Solids **75**, 528 (2014).
[67] W. Tang, E. Sanville, and G. Henkelman, J. Phys.: Condens. Matter **21**, 084204 (2009).
[68] L. Pauling, *The Nature of the Chemical Bond* (Cornell University, Ithaca, 1960).
[69] P. W. Anderson, Phys. Rev. **124**, 41 (1961).
[70] D. M. Newns, Phys. Rev. **178**, 1123 (1969).
[71] V. A. Margulis and E. E. Muryumin, in *Carbon Nanomaterials in Clean Energy Hydrogen Systems*, edited by B. Baranowski, S. Y. Zaginaichenko, D. V. Schur, V. V. Skorokhod, and A. Veziroglu (Springer, Netherlands, 2009).